International Journal of Heat and Mass Transfer 134 (2019) 17–29

Contents lists available at ScienceDirect

International Journal of Heat and Mass Transfer

journal homepage: www.elsevier.com/locate/ijhmt

Numerical simulation of magnetic nanofluid (MNF) film boiling using the VOSET method in presence of a uniform magnetic field

Kaikai Guo [a], Huixiong Li [a,*], Yuan Feng [a], Tai Wang [b], Jianfu Zhao [c]

[a] State Key Laboratory of Multiphase Flow in Power Engineering, Xi'an Jiaotong University, Xi'an 710049, PR China
[b] Department of Power Engineering, North China Electric Power University, Baoding 071003, PR China
[c] National Microgravity Laboratory, Institute of Mechanics, Chinese Academy of Sciences, Beijing 100190, PR China

ARTICLE INFO

Article history:
Received 11 August 2018
Received in revised form 9 December 2018
Accepted 23 December 2018

Keywords:
Magnetic nanofluid (MNF)
Film boiling
VOSET method
Uniform magnetic field

ABSTRACT

A two-dimensional numerical model for solving the problem of incompressible two-phase boiling of a magnetic nanofluid (MNF) in presence of a magnetic field was established by the VOSET (the coupled VOF and a level set method) interface tracking method including a phase change effect. The present work was focused on analyses of the bubble growth and heat transfer characteristics in saturated film boiling at various volume concentrations, magnetic field intensities and magnetic susceptibilities. Under the condition of low volume concentration, the evaluation of the phase interface was mildly influenced, and the heat transfer performance of MNF film boiling was slightly enhanced with an increase in the volume concentration. Discrete bubble growth occurred and the heat transfer characteristics of MNF film boiling were only slightly affected at a lower magnetic field intensity or magnetic susceptibility. In contrast, vapour columns formed and a significant heat transfer enhancement was achieved at a higher magnetic field intensity or magnetic susceptibility.

1. Introduction

A magnetic nanofluid (MNF) is a colloidal suspension in which magnetic nanoparticles coated with a surfactant are steadily dispersed within a base fluid. Base fluids can be water, kerosene, R134a, and so forth. MNFs exhibiting magnetic properties of solid magnetic materials and fluidity of liquids represent a new type of nanoliquid functional materials with a unique performance and wide applications. MNFs exhibit stability without aggregation and deposition under the action of gravity and magnetic field. MNFs demonstrate potential for broad applications and are considered the most promising new intelligent materials in materials science [1]. To date, MNFs have been widely used in chemical engineering, mechanical engineering, medical treatment, instrumentation, environmental protection, navigation, positioning, sealing, etc. As the thermal conductivity of nanoparticles in MNFs can be several orders of magnitude greater than that of the base fluid, the effective thermal conductivity of the MNF is much higher than that of the pure liquid without nanoparticles. In addition, the magnetic nanoparticles in MNF can be controlled by an external magnetic field; thus, the flow field can be controlled and the heat transfer performance of the MNF can be enhanced effectively. Therefore, as a new type of heat transfer medium, MNFs have great practicability in thermal engineering and related fields, such as an energy conversion system controlled by a magnetic field for enhanced heat transfer performance, the cooling system of high power devices, solar collectors, and microelectromechanical systems (MEMS) [1,2].

Boiling heat transfer has been widely used in thermal engineering because of its high heat transfer performance and small temperature difference. To further improve the efficiency of heat exchange equipment and ensure the safety of devices, enhanced boiling heat transfer technology has become an important research subject in modern heat transfer science. In recent years, some researchers have researched the boiling heat transfer characteristics of MNFs and have achieved many important results through combining the advantages of MNFs and boiling heat transfer technology. Liu et al. [3] studied experimentally the pool boiling heat transfer characteristics of a magnetite-water nanofluid (MWNF) with and without a magnetic field. These authors found that magnetic nanoparticles and surfactants can enhance heat transfer performance in the absence of a magnetic field and the heat transfer performance will be further enhanced when an external magnetic field is applied. Lee et al. [4] studied the critical heat flux (CHF) of

* Corresponding author.
E-mail address: huixiong@mail.xjtu.edu.cn (H. Li).

https://doi.org/10.1016/j.ijheatmasstransfer.2018.12.148
0017-9310/

an MWNF and other non-magnetic nanofluids in pool boiling, and their results showed that the MWNF has the highest CHF. Lee et al. [5] further studied the flow boiling heat transfer characteristics of the MNF at atmospheric pressure and low mass flux conditions. These authors found that whether or not an external magnetic field is applied, the CHF of the MNF is still stronger than that of pure water. The researchers analysed the main reasons for CHF enhancement and believed that the magnetic nanoparticles deposited onto the heated surface improve the wetting characteristics of the surface. As the deposition amount of nanoparticles increases, the value of the CHF increases gradually until its saturation value is reached. However, Naphon [6] studied the effect of magnetic fields on the boiling heat transfer characteristics of a cylindrical surface in a nanofluid and obtained a different conclusion then that of Lee [5]. In the absence of a magnetic field, the boiling heat transfer coefficient decreases with an increase in the volume concentration of nanoparticles of the MNF. The main reason is that no surfactant was added to the MNF, which facilitates the continuous gathering of nanoparticles into clusters that are deposited on the heated surface during the boiling process, leading to a further deterioration of the heat transfer on the heated surface. In addition, Naphon also found that under high magnetic field intensity conditions, the maximum heat transfer coefficient of boiling can increase by 27.91%. Sesen et al. [7] believed that in practical applications, the stability of nanofluids is difficult to maintain due to the deposition of nanoparticles onto the surface. To solve this problem, these authors used a magnetic stirrer as a magnetic drive, which not only enhances the cooling capacity of the system but also avoids the aggregation and deposition of the nanoparticles. Afterwards, the researchers used the improved experimental system to study the pool boiling heat transfer characteristics of the MNF. The results showed that this new device enhanced the heat transfer by approximately 17% and the aggregation and deposition of nanoparticles did not occur during the experiment. Abdollahi et al. [8,9] studied the boiling heat transfer characteristics of an Fe_3O_4/DI water nanofluid in presence of a magnetic field. These authors found that when the volume concentration of the MNF increases from zero to 0.1%, the boiling heat transfer coefficient of heated wall gradually increases, then decreases after the volume concentration exceeded 0.1%. The boiling heat transfer coefficient of the MNF with a volume concentration of 0.1% increased by nearly 43% compared with that of DI water. These investigators also found that the direction of the magnetic field gradient has a significant impact on the heat transfer performance of the MNF. When the magnetic field gradient is positive, the boiling heat transfer coefficient decreases. However, the negative magnetic field gradient led to an increase in heat transfer performance. Ultimately, these authors concluded that increasing the volume concentration of nanoparticles and applying magnetic fields are not the only major factors affecting the boiling heat transfer performance. Surface roughness, average nanoparticle size and magnetic field gradient can also significantly influence the heat transfer characteristics of MNF boiling. Amirzehni et al. [10] conducted an experimental study on the subcooled flow boiling of an MWNF in a vertical ascending annular channel in presence of a non-uniform magnetic field, aiming to study the lift-off diameter of the boiling bubble. The experimental results showed that applying a magnetic field can reduce the lift-off diameter by 5–10% and increase the CHF value. In addition to the effect of the magnetic field, the lift-off diameter increases with an increase in the mass velocity.

With the development of numerical methods and the rapid improvement of computer performance, some scholars have already used numerical methods to study the boiling heat transfer characteristics of MNFs. Mohammadpourfard et al. [11] used the mixture model to simulate the pool boiling heat transfer characteristics of an MWNF. These authors determined that when ferromagnetic nanoparticles are added, the pool boiling heat transfer performance is significantly enhanced. When a negative magnetic field gradient is applied, the heat transfer characteristic is further enhanced with an increase in the negative magnetic gradient. Subsequently, Mohammadpourfard et al. [12,13] further studied the subcooled boiling heat transfer characteristics of an R113-based MNF in the vertical annular channel in presence of a non-uniform magnetic field by using a two-fluid model. Their results showed that the use of the MNF as working medium and the application of non-uniform magnetic fields significantly improve the heat transfer performance of boiling. Malvandi et al. [14] conducted a theoretical analysis and research on the film boiling of the MNF on vertical plates. These authors considered the migration of nanoparticles and the effects of the anisotropic thermodynamic properties of the MNF in presence of uniform magnetic fields with varying directions and theoretically modelled the film boiling of the MNF. The following conclusions were obtained. In the case of a high volume concentration, the small nanoparticles increase the velocity distribution in the gas film, while the larger magnetic field intensity reduces the velocity distribution in the gas film. Additionally, under the condition of a low volume concentration, the large nanoparticles enhance the heat transfer performance, and the heat transfer performance is best when the magnetic field is parallel to the temperature gradient. Taheri and Mohammadpourfard [15] used a molecular dynamics model (MD) to conduct a numerical study on the effects of the surface wetting characteristics and nanoparticle concentration on the liquid argon-based MNF boiling heat transfer characteristics in presence of a magnetic field. Their results showed that compared with the pure liquid, the MNF containing hydrophilic nanoparticles are less prone to film boiling, and MNFs containing hydrophobic nanoparticles are more likely to produce gas film. In addition, they believed that an increase in the concentration of nanoparticles or a decrease in the magnetic force changes the momentum transport of fluid particles, leading to an increase in the energy of liquid particles, which changes the boiling nucleation process.

It can be seen from the research results of the above scholars that few investigators have studied the dynamic characteristics of MNF boiling bubbles. As is well known, the dynamic characteristics of bubbles have a very important influence on the boiling heat transfer characteristics. In recent years, great progress has been made in the numerical simulation method for the gas-liquid two-phase flow of MNFs [16–18]; thus, it is possible to study the dynamic characteristics of MNF boiling bubbles by using an interface capture method, such as VOF method, Level-set method, CLSVOF method and VOSET method. However, as well known, the VOF method is not accurate in calculating the direction and curvature of the interface, and the Level-set method is difficult to maintain the conservation of the total mass enclosed in interfaces. Although realizing the combination of VOF method and level-set method and giving full play to the advantages of the two methods, the CLSVOF method needs to solve the advection equation of both the VOF function and the level-set function, which greatly increases the complexity of the algorithm. Sun and Tao [19] proposed the VOSET method also by combining the VOF method and the level-set method, and the VOSET method as well has the advantages of both the VOF method and the level-set method, but the VOSET method does not need to calculate the advection equation of the level-set function separately, but only solves the VOF equation. As a result, the calculation process of the VOSET method is more efficient than that of the CLSVOF method. In this paper, a two-dimensional numerical model for the incompressible two-phase boiling of the MNF will be developed by the VOSET interface capture method to study the heat transfer characteristics of MNF film boiling and the dynamics of bubbles.

2. Numerical modelling

2.1. Governing equations

Because of the complexity of the boiling problem of MNFs, the following assumptions are made in this paper: (1) The magnetic nanoparticles are uniformly dispersed in the base fluid and do not interact with each other. Therefore, a magnetic liquid can be treated as a homogeneous fluid with the same properties in the study of the macroscopic behaviour of the MNF. (2) The volume concentration of the MNF studied in this paper is low, so it is assumed that the volume concentration of the MNF does not change during boiling. (3) The effect of a magnetic field on the physical properties and volume concentration of the MNF are not considered. (4) The MNF is non-conductive, and there is no displacement current in the fluid.

In view of the viscous and incompressible two-phase boiling problems of the MNF in presence of a magnetic field, the governing equations include Maxwell's equation of a static magnetic field, the continuous equation, the momentum equation, the energy equation and the transport equation of phase interface.

In this paper, the MNF is considered a non-conductive fluid, and there is no displacement current in the fluid. Maxwell's equations can be simplified as follows:

$$\nabla \times \boldsymbol{H} = 0 \tag{1}$$

$$\nabla \cdot \boldsymbol{B} = 0 \tag{2}$$

where $\boldsymbol{B}$ is the magnetic flux density and $\boldsymbol{H}$ is the magnetic field intensity. According to the equilibrium magnetization theory, the magnetization $\boldsymbol{M}$ can be expressed as $\boldsymbol{M} = \chi \boldsymbol{H}$. The parameter χ is the magnetic susceptibility in a magnetized material, which is defined as $\chi = \mu/\mu_0 - 1$, μ is the relative permeability and μ_0 is the vacuum permeability. The relationship between $\boldsymbol{B}$ and $\boldsymbol{H}$ is as follows:

$$\boldsymbol{B} = \mu_0(1+\chi)\boldsymbol{H} = \mu \boldsymbol{H} \tag{3}$$

Since the curl of the $\boldsymbol{H}$ field is zero, $\boldsymbol{H}$ has the potential function. By introducing the scalar magnetic potential ψ and defining $\boldsymbol{H} = -\nabla\psi$, Maxwell's Eqs. (1) and (2) are further simplified into the Laplace equation concerning the magnetic potential ψ, which is expressed as:

$$\nabla \cdot (\mu \nabla \psi) = 0 \tag{4}$$

It can be seen that only the spatial distribution of the magnetic potential ψ is required. According to $\boldsymbol{H} = -\nabla\psi$ and the relationship between $\boldsymbol{B}$ and $\boldsymbol{H}$, the spatial distribution of the magnetic field intensity $\boldsymbol{H}$ can be easily obtained. In addition, the value of ψ depends on μ. However, μ is a different constant in each phase but changes at the phase interface, which indicates that the distribution of ψ will change correspondingly with the evolution of the phase interface. At the phase interface of the MNF, the magnetic field satisfies certain boundary conditions. $\boldsymbol{B}$ is continuous in the normal direction of the phase interface, and $\boldsymbol{H}$ is continuous in the tangential direction of the phase interface. That is, $\boldsymbol{B}_1$, $\boldsymbol{H}_1$, $\boldsymbol{B}_2$ and $\boldsymbol{H}_2$ on both sides of the phase interface can be expressed as the following expressions:

$$\boldsymbol{n} \cdot (\boldsymbol{B}_1 - \boldsymbol{B}_2) = 0 \tag{5}$$

$$\boldsymbol{n} \times (\boldsymbol{H}_1 - \boldsymbol{H}_2) = 0 \tag{6}$$

The fluid is assumed to be viscous and incompressible in this paper, in which the physical property is set to be constant. The expression of the two-phase flow governing equations for the boiling can be written as:

$$\nabla \cdot \boldsymbol{u} = \dot{\mathrm{m}}\left(\frac{1}{\rho_{\mathrm{g}}} - \frac{1}{\rho_{\mathrm{l}}}\right) \tag{7}$$

$$\rho\left(\frac{\partial \boldsymbol{u}}{\partial \mathrm{t}} + \boldsymbol{u}\cdot\nabla\boldsymbol{u}\right) = -\nabla \mathrm{p} + \nabla\cdot\left[\eta\left((\nabla\boldsymbol{u}) + (\nabla\boldsymbol{u})^{\mathrm{T}}\right)\right] + \rho\boldsymbol{g}(1-\beta_{\mathrm{T}}(\mathrm{T}-\mathrm{T}_{\mathrm{sat}})) + \boldsymbol{F}_{\mathrm{s}} + \boldsymbol{F}_{\mathrm{m}} \tag{8}$$

$$\frac{\partial \mathrm{T}}{\partial \mathrm{t}} + \boldsymbol{u}\cdot\nabla\mathrm{T} = \frac{\mathrm{k}}{\rho \mathrm{C}_{\mathrm{p}}}\nabla^2\mathrm{T} \tag{9}$$

$$\frac{\partial \mathrm{c}}{\partial \mathrm{t}} + \boldsymbol{u}\cdot\nabla\mathrm{c} = \frac{\dot{\mathrm{m}}}{\rho_{\mathrm{g}}} \tag{10}$$

where ρ, $\boldsymbol{u}$, p, η, $\boldsymbol{g}$, T, k and C_p represent the density, velocity, pressure, viscosity, gravitational acceleration, temperature, thermal conductivity and specific heat, respectively. The parameter c is a function of the VOF, which varies between 0 and 1, $\dot{m}$ denotes the mass transfer rate produced by evaporation at the phase interface, β_T is the coefficient of volumetric expansion, T_{sat} is the saturation temperature of the liquid phase, $\boldsymbol{F}_s$ is the surface tension and $\boldsymbol{F}_m$ is the magnetic force. It was assumed that the temperature of the liquid phase and the phase interface are the saturated temperature, and the gas phase temperature is solved by using the single-phase temperature Eq. (9). $\boldsymbol{F}_s$ is written as the source term in the momentum equation using a CSF model [20], which is defined as following

$$\boldsymbol{F}_s = -\sigma\kappa(\phi)\delta(\phi)\nabla\phi \tag{11}$$

where σ is the surface tension coefficient, ϕ is the level set function, $\kappa(\phi)$ is the interface curvature and $\delta(\phi)$ is the Dirac delta function. $\kappa(\phi)$ and $\delta(\phi)$ can be defined as follows:

$$\kappa(\phi) = \nabla\cdot\left(\frac{\nabla\phi}{|\nabla\phi|}\right) \tag{12}$$

$$\delta(\phi) = \begin{cases} 0 & \text{when } |\phi| > \boldsymbol{s} \\ \frac{1}{2\boldsymbol{s}}\left[1+\cos\left(\frac{\pi\phi}{\boldsymbol{s}}\right)\right] & \text{when } |\phi| \leqslant \boldsymbol{s} \end{cases} \tag{13}$$

where s is the width of the smooth areas between both sides of the phase interface, which is defined as $s = 1.5\,h$. The parameter h is the grid size.

For incompressible, isothermal and linear magnetic materials, $\boldsymbol{F}_m$ can be calculated according to the method proposed by Rosensweig [21], which can be written as:

$$\boldsymbol{F}_{\mathrm{m}} = -\frac{1}{2}\mathrm{H}^2\nabla\mu \tag{14}$$

The level set function is substituted into Eq. (14), and Eq. (14) can be further written as:

$$\boldsymbol{F}_{\mathrm{m}} = -\frac{1}{2}\mathrm{H}^2\left(\mu_{\mathrm{l}} - \mu_{\mathrm{g}}\right)\delta(\phi)\nabla\phi \tag{15}$$

2.2. Physical property of the MNF

It is assumed that there is a local thermal balance and no slip between the magnetic nanoparticles and the substrate. A MNF can be approximately considered a single-phase fluid [21]. The physical property of the MNF can be obtained from the physical parameters of the nanoparticles and base fluids, which are calculated as follows [21]:

$$\text{Density}: \quad \rho_{\mathrm{mix}} = (1-\varphi)\rho_{\mathrm{l}} + \varphi\rho_{\mathrm{p}} \tag{16}$$

$$\text{Specific heat}: \quad \mathrm{c}_{\mathrm{p,mix}} = \frac{(1-\varphi)\rho_{\mathrm{l}}\mathrm{c}_{\mathrm{p},l} + \varphi\rho_{\mathrm{p}}\mathrm{c}_{\mathrm{p,p}}}{\rho_{\mathrm{mix}}} \tag{17}$$

$$\text{Thermal conductivity}: \quad k_{mix} = \left(\frac{k_p + 2k_l - 2\varphi(k_l - k_p)}{k_p + 2k_l + \varphi(k_l - k_p)}\right)k_l \tag{18}$$

$$\text{Dynamic viscosity}: \quad \eta_{mix} = (1 + 2.5\varphi)\eta_l \tag{19}$$

where φ is the volume concentration of the MNF.

2.3. Interface tracking

The liquid-vapour interface is captured by a VOSET method, a coupled VOF and a level set method proposed by Sun and Tao [19]. First, the VOF equation is solved by using the Youngs-PLIC method, and the normal direction of phase interface is obtained. After the geometric reconstruction of the initial phase interface shape and position, the level set function is calculated using the geometric method proposed by Wang [22]. Details of the treatment of the VOSET method are provided in the literature [19,22]. After obtaining the level set function, the density ρ, viscosity η and magnetic permeability μ are given by:

$$\rho(\phi) = \rho_g \boldsymbol{H}(\phi) + \rho_l(1 - \boldsymbol{H}(\phi)) \tag{20}$$

$$\eta(\phi) = \eta_g \boldsymbol{H}(\phi) + \eta_l(1 - \boldsymbol{H}(\phi)) \tag{21}$$

$$\mu(\phi) = \mu_g \boldsymbol{H}(\phi) + \mu_l(1 - \boldsymbol{H}(\phi)) \tag{22}$$

where $H(\phi)$ is the smooth Heaviside function and can be written as:

$$\boldsymbol{H}(\phi) = \begin{cases} 0 & \text{when } \phi < -\boldsymbol{s} \\ \frac{1}{2}\left[1 + \frac{\phi}{\boldsymbol{s}} + \frac{1}{\pi}\sin\left(\frac{\pi\phi}{\boldsymbol{s}}\right)\right] & \text{when } |\phi| < \boldsymbol{s} \\ 1 & \text{when } \phi > \boldsymbol{s} \end{cases} \tag{23}$$

2.4. Solving governing equations

The governing equations are discretized by the finite volume method based on a collocated grid in the present study. The convection term adopts the QUICK format, the diffusion term adopts the central difference format, and finally, the discrete equations are solved by the alternating direction implicit iteration method (ADI method). The unsteady IDEAL algorithm [23] is adopted to address the coupling of the pressure and velocity.

In this paper, Ling et al.'s processing method [24] is used to solve the temperature of the grid unit containing the phase interface, as shown Fig. 1. For a unit containing a phase interface, the temperature is calculated using the linear interpolation in the normal direction of the phase interface. If the centre of the phase interface grid is located in the liquid phase, the temperature of this unit can be set as the saturation temperature. If the centre of the grid is located in the gas phase, interpolation point A′ is sought along the normal direction of the phase interface. The distance between point A′ and grid centre point A is 1.5 times the grid size. The temperature of grid centre point A is estimated according to the distance between these two points and the phase interface, as shown in the following equation:

$$\left|\frac{\boldsymbol{T}_A - \boldsymbol{T}_{sat}}{\boldsymbol{T}_{A'} - \boldsymbol{T}_{sat}}\right| = \frac{|\phi_A|}{|\phi_A| + \boldsymbol{d}} \tag{24}$$

where d is 1.5 times the grid size. The temperature of the point A′ is obtained by a bilinear interpolation from nearby cells. The function ϕ_A is the level set function of cell A, and its absolute value equals the distance between the point A and the phase interface. Ling et al. [24] provides the temperature solution details of the grid cell containing the phase interface.

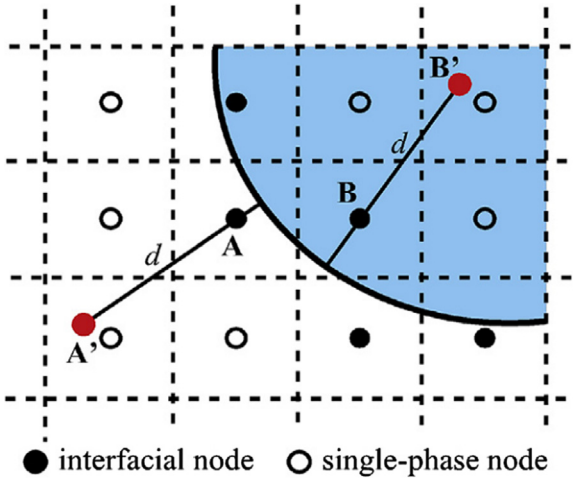

Fig. 1. The method solving the temperature field with an immersed boundary condition at the interface [24].

2.5. Solving the interfacial mass transfer rate $\dot{m}$

If we assume that dV is the volume of the control unit Ω and dA is the area of the gas-liquid interface Γ, then the following relationship needs to be satisfied:

$$\int_\Omega \dot{\boldsymbol{m}} d\boldsymbol{V} = \frac{1}{\gamma}\int_\Gamma \dot{\boldsymbol{q}} d\boldsymbol{A} \tag{25}$$

where γ is the latent heat of evaporation and $\dot{q}$ refers to the heat flux flowing into the interface, as shown:

$$\dot{\boldsymbol{q}} = \boldsymbol{k}_g \frac{\partial \boldsymbol{T}}{\partial \boldsymbol{n}}\bigg|_g - \boldsymbol{k}_l \frac{\partial \boldsymbol{T}}{\partial \boldsymbol{n}}\bigg|_l \tag{26}$$

In this paper, a normal probe technique proposed by Udaykumar [25] and bilinear interpolation method are used to calculate the temperature gradient on both sides of the phase interface. The detailed solution process can be found in the literature [24,25]. If the temperature gradient on both sides of the phase interface is obtained, then the mass transfer rate can be calculated by the following formula:

$$\int_\Omega \dot{\boldsymbol{m}} d\boldsymbol{V} = \frac{1}{\gamma}\left(\boldsymbol{k}_g \frac{\partial \boldsymbol{T}}{\partial \boldsymbol{n}}\bigg|_g - \boldsymbol{k}_l \frac{\partial \boldsymbol{T}}{\partial \boldsymbol{n}}\bigg|_l\right)\Delta \boldsymbol{A} \tag{27}$$

where ΔA is the area of the phase interface of the grid cell containing phase interface, which can be obtained by a geometric method.

2.6. Boundary conditions

The physical properties of the fluid and the magnetic nanoparticles used in this paper are shown in Table 1. The Taylor instability wavelength of film boiling is $\lambda_0 = 2\pi\,(3\sigma/(g/(\rho_l - \rho_g)))^{-1/2}$ in 2-D. To ensure that the fluid is in a uniform magnetic field and avoid that the magnetic field boundary affects the flow field, the computational region is divided into two regions. The magnetic field is

Table 1
The physical properties of the MNF used in this study.

	Liquid	Vapour	Nanoparticle
Density (kg/m^3)	200.0	5.0	5600.0
Thermal conductivity (W/m·K)	40.0	1.0	6.0
Thermal capacity (J/kg·K)	400.0	200	670.0
Dynamic viscosity (kg/m·s)	0.1	0.005	
Surface tension coefficient (N/m)	0.1		
Latent heat (J/kg)	10000.0		
Magnetic susceptibility	0.2/0.4/0.8		

solved in region **I** (EFGH), and the flow field is solved in region **II** (ABCD), as shown in Fig. 2. The computational domain for solving the magnetic field is chosen to be $3\lambda_0 \times 5\lambda_0$ and that for solving the flow field is chosen to be $3\lambda_0 \times 3\lambda_0$. According to the gas - liquid interface obtained from region **II**, region **I** is calculated until region **I** is stable, and region **I** and region **II** are simultaneously solved by a coupling iteration approach.

Symmetry conditions are provided at the left and right boundaries both regions **I** and **II** as

$$\begin{aligned} &\boldsymbol{ABCD}: \quad \boldsymbol{u}=0, \frac{\partial \boldsymbol{v}}{\partial \boldsymbol{x}}=0, \frac{\partial \boldsymbol{T}}{\partial \boldsymbol{x}}=0 \\ &\boldsymbol{EFGH}: \quad \frac{\partial \psi}{\partial \boldsymbol{x}}=0 \end{aligned} \tag{28}$$

The top wall of region **I** is explicitly defined at a constant magnetic field intensity and outflow condition is incorporated at the top boundary of region **II**. The conditions are mentioned as follows:

$$\begin{aligned} &\boldsymbol{ABCD}: \quad \frac{\partial \boldsymbol{u}}{\partial \boldsymbol{y}}=\frac{\partial \boldsymbol{v}}{\partial \boldsymbol{y}}=\frac{\partial \boldsymbol{T}}{\partial \boldsymbol{y}}=0 \\ &\boldsymbol{EFGH}: \quad \frac{\partial \psi}{\partial \boldsymbol{y}}=-\frac{\mu_0}{\mu_g}\boldsymbol{H}_0 \end{aligned} \tag{29}$$

The bottom wall of region **I** is explicitly defined at a constant magnetic field intensity. A constant heat flux and a no-slip wall condition are incorporated at the bottom boundary of region **II**. The conditions are defined as follows:

$$\begin{aligned} &\boldsymbol{ABCD}: \quad \boldsymbol{u}=\boldsymbol{v}=0, -\boldsymbol{k}_g\frac{\partial \boldsymbol{T}}{\partial \boldsymbol{y}}=\boldsymbol{q}_w \\ &\boldsymbol{EFGH}: \quad \frac{\partial \psi}{\partial \boldsymbol{y}}=\frac{\mu_0}{\mu_g}\boldsymbol{H}_0 \end{aligned} \tag{30}$$

2.7. Variable time step size

Due to the requirement of computation stability, the time step used in the numerical simulation should be limited to small values. According to [26], the restrictions to time step is usually taken as $\Delta \boldsymbol{t} \leqslant 0.8\rho_l \boldsymbol{h}^2/(6\mu_l)$, $\Delta \boldsymbol{t} \leqslant 0.8\rho_v \boldsymbol{h}^2/(6\mu_v)$, $\Delta \boldsymbol{t} \leqslant 0.5\sqrt{(\rho_l+\rho_v)\boldsymbol{h}^3/(\pi\sigma)}$ and $\Delta \boldsymbol{t} \leqslant 0.1\boldsymbol{h}/\mathrm{u}_{\max}$, where h is the mesh size and u_{max} is the maximum velocity in the flow field. An upper limit of 10^{-4} s to the time step was adopted in the present study.

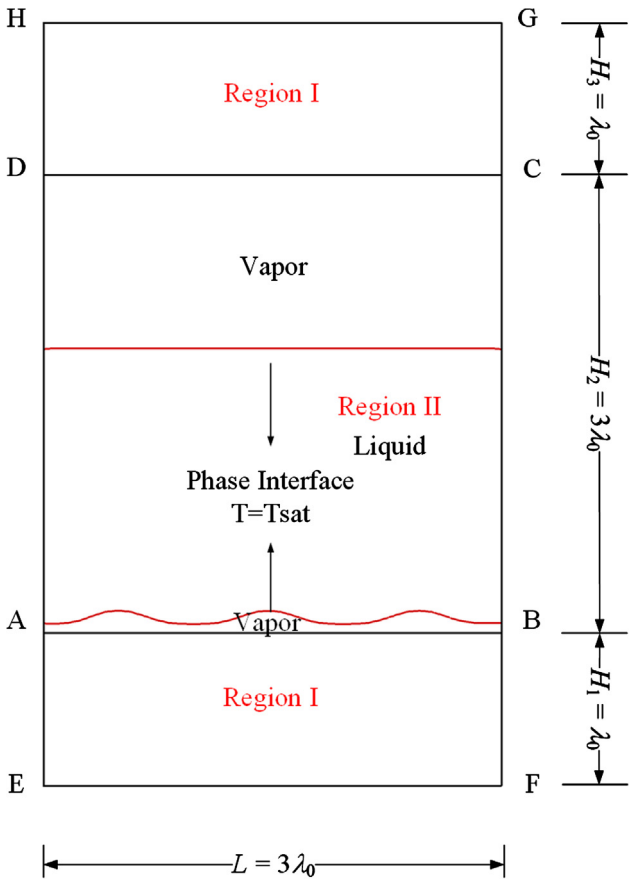

Fig. 2. Computational domain for the MNF film boiling simulation.

3. Numerical method validation

3.1. Magnetic field validation

First, the accuracy of the numerical solution of Maxwell's equations was verified. In this paper, the numerical solution of the magnetic potential equation was verified by taking the distribution of a magnetic field around an infinitely long stationary cylinder. In a uniform magnetic field, the theoretical solution to the distribution of the magnetic field around an infinitely long stationary cylinder [27] is shown below:

$$\boldsymbol{H}=\begin{cases} -\mathrm{A}(\boldsymbol{e}_\mathrm{r}\sin\theta+\boldsymbol{e}_\theta\cos\theta), & \mathrm{r}\leqslant \mathrm{R} \\ -(\mathrm{E}-\mathrm{D}/\mathrm{r}^2)\sin\theta\boldsymbol{e}_\mathrm{r}-(\mathrm{E}+\mathrm{D}/\mathrm{r}^2)\cos\theta\boldsymbol{e}_\theta, & \mathrm{r}>\mathrm{R} \end{cases} \tag{31}$$

The magnetic field at infinity ($r \to \infty$) is uniform, and $\boldsymbol{H} = \mathrm{H}_0\boldsymbol{j}$, where $\boldsymbol{j} = \boldsymbol{e}_r\sin\theta + \boldsymbol{e}_\theta\cos\theta$. $\boldsymbol{j}$ is the unit vector in the y direction. In Eq. (31),

$$\boldsymbol{E}=-\boldsymbol{H}_0, \quad \boldsymbol{A}=-\frac{2\mu_2\boldsymbol{H}_0}{\mu_1+\mu_2}, \quad \boldsymbol{D}=\frac{\mu_1-\mu_2}{\mu_1+\mu_2}\boldsymbol{R}^2\boldsymbol{H}_0$$

The detailed parameters of the validation example in this present study are shown as follows: the computational domain is chosen to be $10R \times 10R$ with $R = 0.002$ m, the whole computational domain is discretized by a uniform 200×200 grid ($R/\Delta = 20$), the magnetic permeability within the cylinder is $\mu_1 = 2\mu_0$, the magnetic permeability outside the cylinder is $\mu_2 = \mu_0$, and the applied uniform magnetic field is vertical with an intensity of $H_0 = 1.0$ kA/m. Fig. 3(a) presents the contrast between the numerical and theoretical solutions of the magnetic field intensity on the centre line of $x = 0.01$ m. From Eq. (31), the theoretical value of the magnetic field intensity within the circle is 0.667 kA/m, and the magnetic field intensity within the circle obtained by numerical simulation is 0.661 kA/m. The relative error between the numerical solution and the theoretical solution is 0.9%, which shows that the results are basically consistent with each other, indicating that the solution of Maxwell's equations in this present study is very accurate.

Subsequently, the numerical model of MNF two-phase flow was validated. In this paper, the equilibrium shape of a gravity-free MNF droplet in a uniform magnetic field was simulated numerically, and the calculated results were compared with the experimental results of Flament et al. [28]. In this study, a stationary circular MNF droplet with radius $R = 0.001$ m was located at the centre of a domain of $8R \times 8R$. The density, viscosity, and magnetic permeability of the MNF droplet were $\rho_d = 1380$ kg/m^3, $\eta_d = 6.64$ mPa·s and $\mu_d = 3.2\mu_0$, respectively. The surrounding fluid was non-magnetic having a magnetic permeability close to the vacuum μ_0. The density, viscosity and surface tension coefficient of nonmagnetic fluid are $\rho_c = 800$ kg/m^3, $\eta_c = 3.81$ mPa·s and $\sigma = 3.07$ mN/m, respectively. A uniform magnetic field was applied from the bottom to the top, and the gravity was not considered. No slip boundary condition was applied on all walls, and the continuity of the normal $\boldsymbol{B}$ and the tangential $\boldsymbol{H}$ was the magnetic field boundary condition. A mesh number of 128×128 ($R/\Delta = 16$) was applied.

The ratio of the long axis a and short axis b in the directions parallel and perpendicular to the magnetic field a/b is defined to represent the deformation degree of the droplet. Fig. 3(b) shows the value of a/b in presence of different magnetic field intensities, indi-

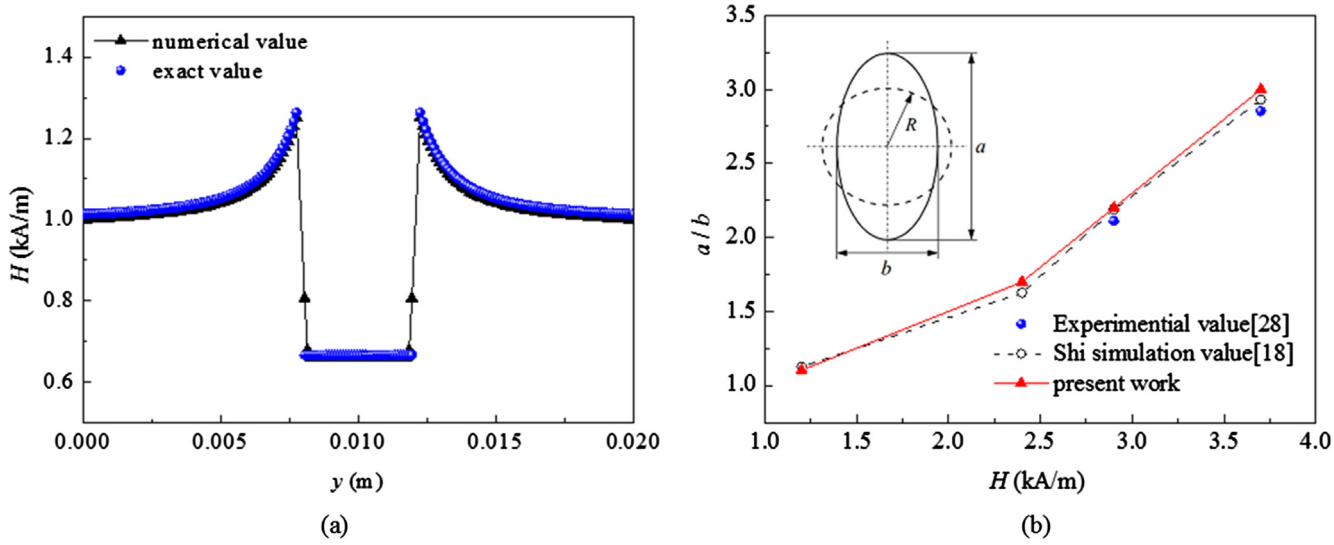

Fig. 3. (a) The contrast between the numerical and theoretical solutions of the magnetic field intensity on the centre line of $x = 0.01$ m. (b) The value of a/b in presence of different magnetic field intensities.

cating that with an increase in the magnetic field intensity, the droplet is stretched along the magnetic field direction, and the stronger the magnetic field, the greater the deformation. Clearly, in Fig. 3(b), the calculation results in this paper are in good agreement with the calculation results of Shi et al. [18] and the experimental results of Flament et al. [28]. This excellent agreement indicates that the current model developed in this paper can be used to accurately study the incompressible two-phase flow of MNFs in presence of the magnetic fields.

3.2. Saturated film boiling validation of a pure fluid without a magnetic field

Two-dimensional horizontal saturated film boiling was simulated to evaluate the accuracy of the numerical method described in part **2**. In this case, the volume concentration and magnetic field intensity of the MNF were both zero. The physical properties of the liquid and gas used in this study are shown in Table 1. The interface location was initialized as $y(x) = 1/128\lambda_0(4.0 + \cos(2\pi x/\lambda_0))$. The liquid was initialized to be in a saturation state, and the vapour temperature increased linearly from the liquid–vapour interface to the wall.

To obtain reasonable calculation results, a mesh independency study is required. In this study, the heat flux, magnetic field intensity and volume concentration are $q_w = 1$ kW/m^2, $H_0 = 0$ kA/m and $\varphi = 0\%$, respectively. Three different grid sizes of $\lambda_0/32$, $\lambda_0/64$ and $\lambda_0/128$ were adopted for this simulation. Fig. 4 shows the terminal shape of the phase interface obtained under different grid sizes at 0.45 s, indicating that the shape of the phase interface did not significantly change when the grid was finer than $\lambda_0/64$. Furthermore, when the grid sizes were $\lambda_0/32$, $\lambda_0/64$ and $\lambda_0/128$, the gas volumes were 2.5115E−3 m^3, 2.5901E−3 m^3 and 2.614E−3 m^3, respectively. The difference between the gas volumes at $\lambda_0/32$ and $\lambda_0/64$ was 3.15% and that between the gas volumes at $\lambda_0/64$ and $\lambda_0/128$ was 0.92%. According to the above results, a grid resolution of $\lambda_0/64$ has the adequate numerical accuracy.

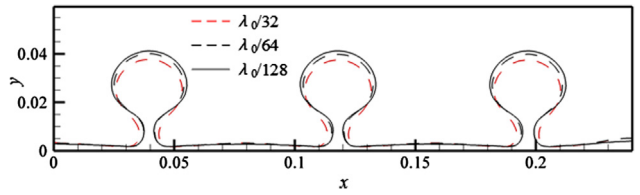

Fig. 4. The terminal shape of the phase interface with different grid sizes at 0.45 s.

In order to check the effect of the time step on the computation results, a series of computations were carried out with the time step of $\Delta t = 10^{-4}$ s, $\Delta t = 10^{-5}$ s and half of original time step size to conduct the computation on the problem studied in the grid independence test once more in the $\lambda_0/64$ grid. Fig. 5 shows the evolution of bubble rising velocities with time as well as that by the original time step. These four lines almost coincide, indicating that the time step used in the present simulations are small enough.

The spatial average Nusselt number in film boiling can be defined as

$$\mathrm{Nu} = \frac{1}{\lambda_0}\int_0^{\lambda_0} \mathrm{Nu}'\boldsymbol{dx} \tag{32}$$

where Nu′ is the local Nusselt number, which is written as

$$\mathrm{Nu}' = \frac{\boldsymbol{l}_0}{\boldsymbol{T}_w - \boldsymbol{T}_{sat}}\left.\frac{\partial \boldsymbol{T}}{\partial \boldsymbol{y}}\right|_{y=0}, \quad \text{where } l_0 = \sqrt{\frac{\sigma}{\left(\rho_l - \rho_g\right)\boldsymbol{g}}} \tag{33}$$

At present, there are many correlations that describe the complex mechanism of horizontal film boiling, among which Klimenko's correlation [29] has been widely used. Fig. 6 shows the

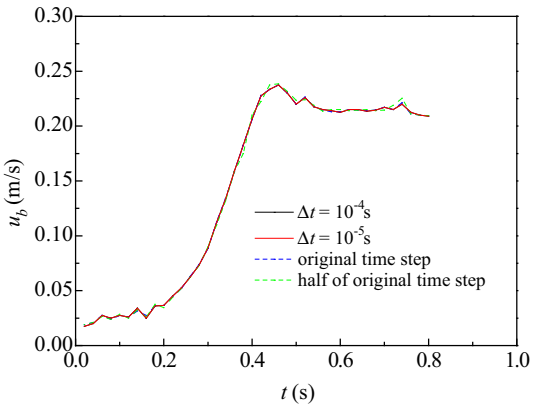

Fig. 5. Bubble rising velocity obtained by different time steps in grid size of $\lambda_0/64$.

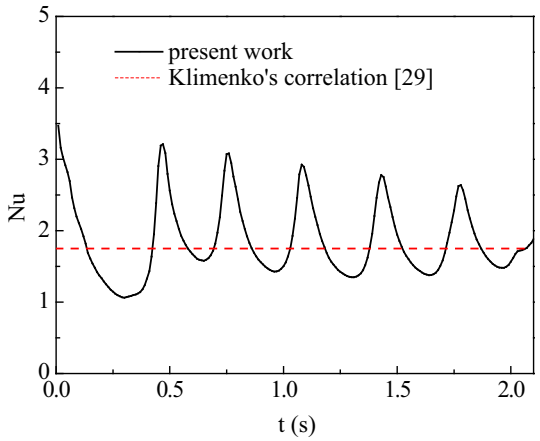

Fig. 6. The spatial average Nu number with time when $q_w = 1$ kW/m^2.

changing trend of the spatial average Nu number with time when $q_w = 1$ kW/m^2, which reveals the cycling characteristics of bubble growth and release in the computational domain. The spatial and temporal average Nu number obtained by the numerical simulation is 1.85, while that obtained by Klimenko's correlation was 1.75, and the difference between the two is 5.7%. It can be seen from the comparison results that the numerical simulation results are in good agreement with the experimental correlation results, which verifies the accuracy of the two-phase boiling model in this paper.

4. Results and discussion

In this section, the developed numerical model in this paper is used to simulate the heat transfer characteristics of saturated film boiling of the MNF and the dynamic characteristics of boiling bubbles under different volume concentrations, magnetic field intensities and magnetic susceptibilities in the presence of a uniform magnetic field.

4.1. Effect of concentration

First, the effects of volume concentration on the heat transfer characteristics of MNF film boiling without a magnetic field were studied. Fig. 7(a) and (b) show the change in the spatial average wall temperature and the spatial average Nu number with time at different volume concentrations, respectively. Fig. 8 shows the interface shape when a bubble is released at different volume concentrations. In Fig. 7(a) and (b), with an increase in volume concentration, the spatial average temperature and the spatial average Nu of the bottom wall change periodically with time. The number of valleys of the wall temperature and peaks of Nu represent the number of times a bubble is released. When the volume concentration increases from 0 to 0.2%, there is no significant change in the period and amplitude, and there are five valleys of the wall temperature and five peaks of Nu, revealing that five bubbles are detached during the simulated time, as shown in Fig. 8 (a)∼(c). When the volume concentration is further increased, the bubble departure times of $\varphi = 0.4\%$, $\varphi = 0.8\%$ and $\varphi = 1.2\%$ are six in the total time. However, as shown in Fig. 7(a) and (b), when the volume concentration increases from 0.4% to 1.2%, although the number of released bubbles is the same, the valley value of the wall temperature and the peak value of Nu both advance. An increase in the volume concentration shortens the detaching time of a bubble and accelerates bubble departure to some extent, as displayed in Fig. 8(d)∼(f). Fig. 9 shows the changes in the space- and time-averaged wall temperature and the space- and time-averaged Nu with volume concentration. Under the condition of a low volume concentration, the space- and time-averaged wall temperature decreases, and the space- and time-averaged Nu number increases with an increase in volume concentration. These results indicate that increasing the volume concentration can improve the heat transfer performance of the MNF to some extent under the condition of a low volume concentration.

4.2. Effect of the magnetic field intensity

The magnetic field intensity can directly influence the magnetic force acting on the bubble, which will further affect the dynamic characteristic of the bubble. Fig. 10 shows the distributions of magnetic streamlines and magnetic field force at 0.4 s under conditions with $H_0 = 10$ kA/m and $\chi = 0.2$. As seen in Fig. 10(a), the vertical upward magnetic field is applied in the computational domain, and as seen in Fig. 10(b) the magnetic field force acted on the bubble has the same direction as that of the surface tension due to the fact that the ratio of the magnetic permittivity of the liquid to that of the vapour is greater than 1. Fig. 11 shows the velocity vector,

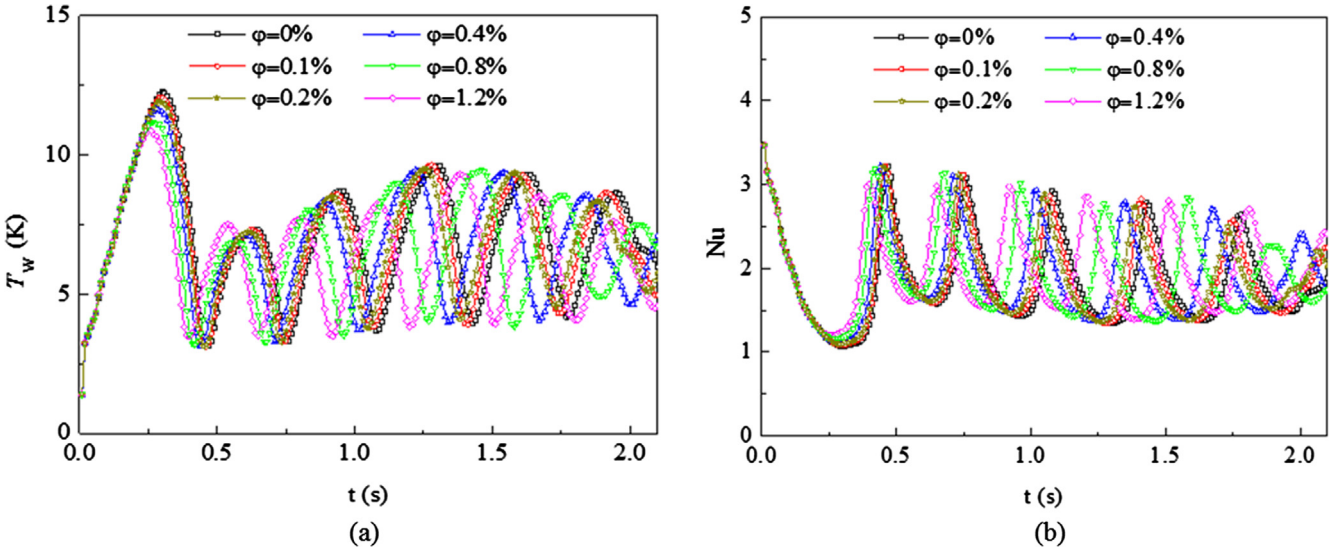

Fig. 7. Variation in the space-averaged (a) wall temperature and (b) Nusselt number for different volume concentrations of the MNF.

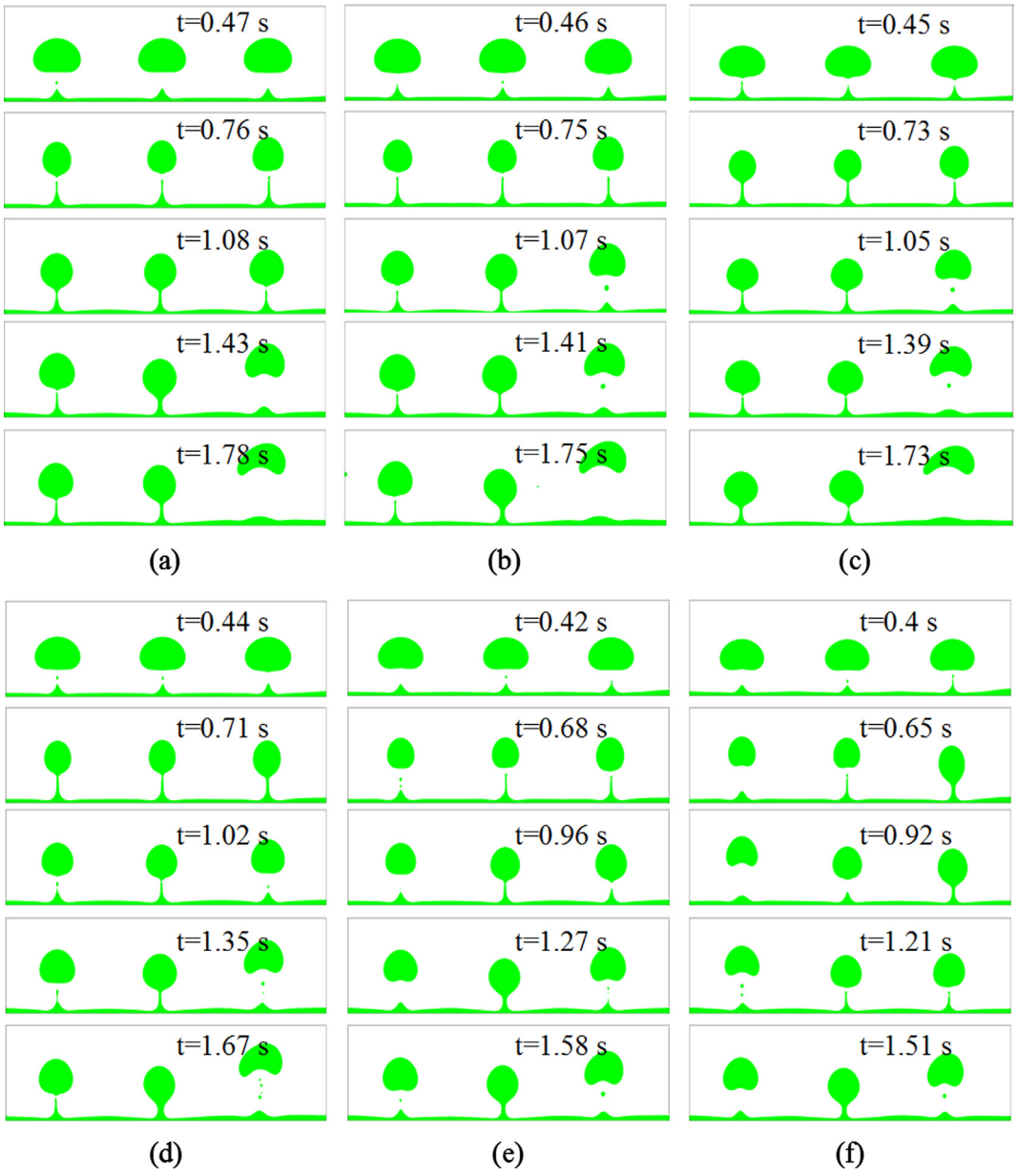

Fig. 8. Interface growth for bubble release with different volume concentrations of the MNF: (a) φ = 0%; (b) φ = 0.1%; (c) φ = 0.2%; (d) φ = 0.4%; (e) φ = 0.8% and (f) φ = 1.2%.

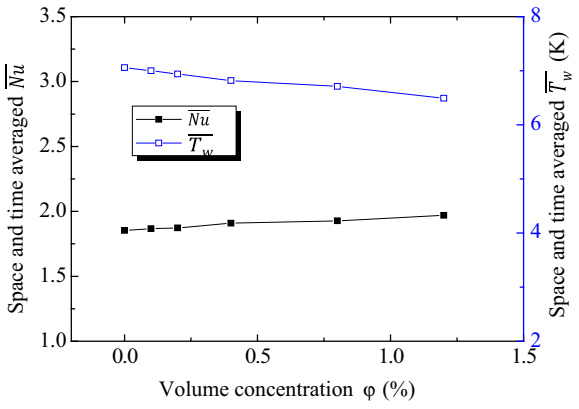

Fig. 9. The space- and time-averaged Nusselt number and wall temperature with different volume concentrations of the MNF.

magnetic field intensity contours and also the temperature contour at 0.4 s under conditions of H_0 = 10 kA/m and H_0 = 20 kA/m. It can be seen in Fig. 11 that the evaporation occurs mostly at the base of the vapour columns where the vapour film is closest to the heated surface. It can also be seen in Fig. 11 that the magnetic field intensity gradient is the largest at the phase interface where the phase change occurs, and the stronger the magnetic field intensity, the greater the magnetic field force, and then the faster the bubble disengages due to the larger pressure difference.

Fig. 12 displays the morphology of the phase interface when the bubble first releases with different magnetic field intensities. When the magnetic field intensity is low, such as 5 kA/m and 10 kA/m, the morphology of the phase interface during departure does not significantly change. As the magnetic field intensity increases, the magnetic force on the bubble increases gradually and the bubble begins to deform along the magnetic field direction. The bottom of the bubble gradually becomes sharp, and the bubble departure diameter decreases. When the magnetic field intensity

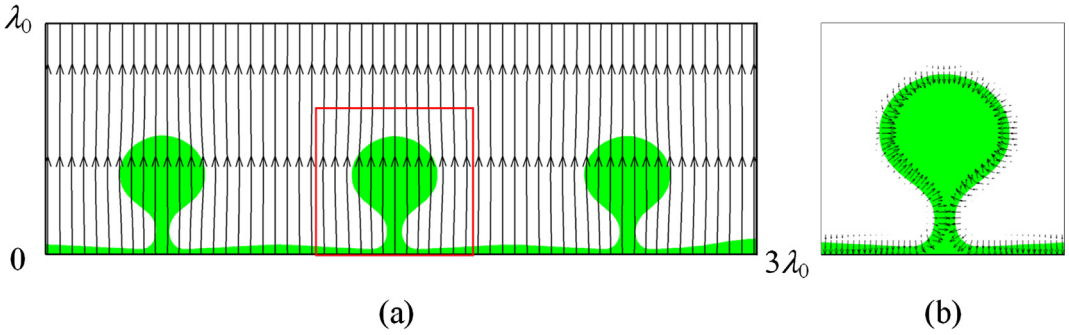

Fig. 10. Distributions of (a) magnetic streamlines and (b) magnetic field force at 0.4 s when H_0 = 10 kA/m.

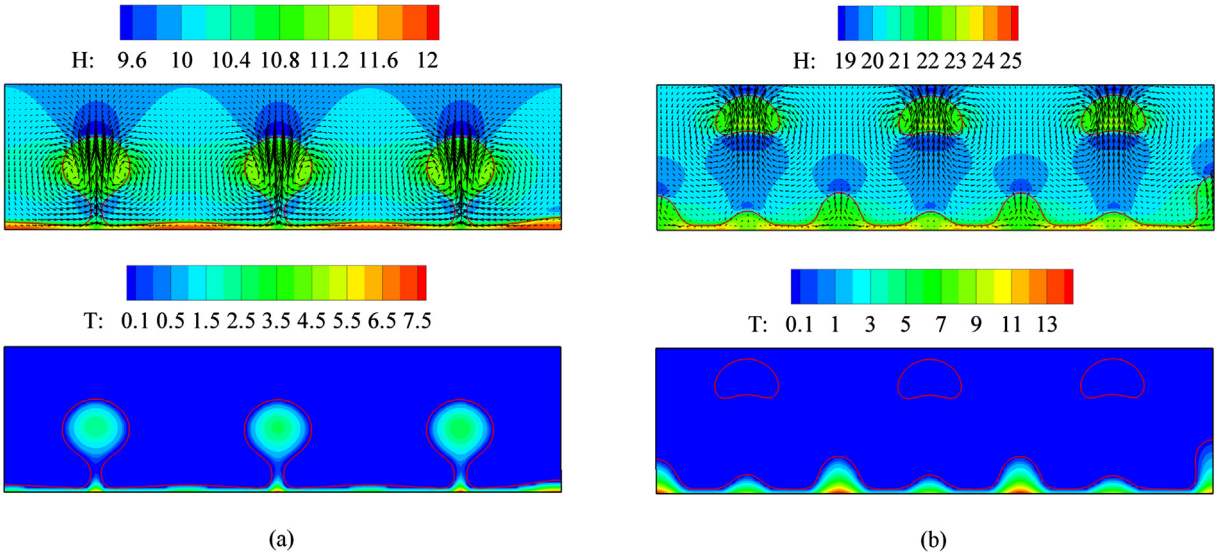

Fig. 11. Velocity vector, magnetic field intensity contours and temperature profile at 0.4 s when (a) H_0 = 10 kA/m and (b) H_0 = 20 kA/m.

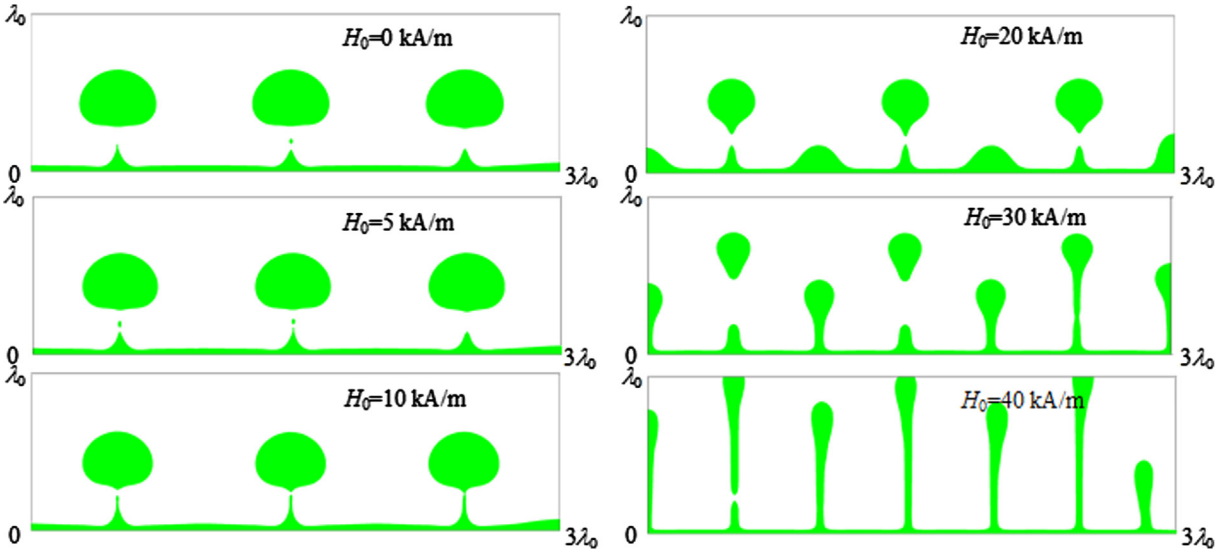

Fig. 12. Interface profiles for the first set of bubble releases with different applied magnetic field intensities.

increases to 40 kA/m, the bubble is stretched along the magnetic field direction under the action of the magnetic force, then a vertical bubble column forms. In addition, an increasing magnetic field intensity causes greater Maxwell stress, which results in greater instability at the gas-liquid interface, a changing wavelength of the vapour film and several bubble formation sites. When the magnetic field intensity is 5 kA/m or 10 kA/m, the magnetic force is small, but the number of bubble formation sites and the wave-

length of the vapour film are basically unchanged. When the magnetic field intensity is further increased to 20 kA/m, 30 kA/m or 40 kA/m, the number of bubble formation sites increases, and the wavelength of the vapour film decreases due to the larger magnetic force. Fig. 13 shows the bubble departure time of the first set of bubble releases with different applied magnetic field intensities. As the magnetic field intensity increases, the magnetic force on the bubble increases, resulting in a decrease in the bubble departure time. When the magnetic field intensity increases to 40 kA/m, the larger magnetic force changes the morphology of the bubble, and the stable vapour column starts to form. Under the action of the magnetic force, the bubble column is gradually stretched and finally breaks off.

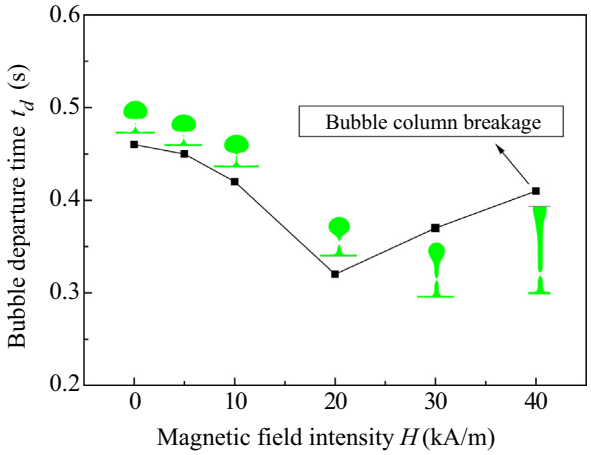

Fig. 13. Bubble departure time for the first set of bubble releases with different applied magnetic field intensities.

The evolution of the phase interface under different magnetic field intensities is shown in Fig. 14. When the magnetic field intensity increases from 0 kA/m to 5 kA/m, the film boiling arrives at the quasi-steady stage after the first departure of the bubble, and the bubble is periodically formed and detached in the same way, as shown in Fig. 14(a)~(b). When the magnetic field intensity further increases to 10 kA/m, the bubble detaches in a similar way to the previous two cases during the initial stage. However, the greater magnetic force causes greater phase interface instability after the initial bubble departure. Therefore, although there is no change in the way the bubble detaches, the number of bubble formation sites increases. When t = 1.07 s, a wave peak appears at the right boundary of the computational domain, followed by a bubble releasing from the location of the peak, as shown in Fig. 14(c). When the magnetic field intensity increases to 20 kA/m, the greater magnetic force will further increase the instability of the phase interface, making the formation and departure of bubbles random and aperiodic. Furthermore, when the number of bubble

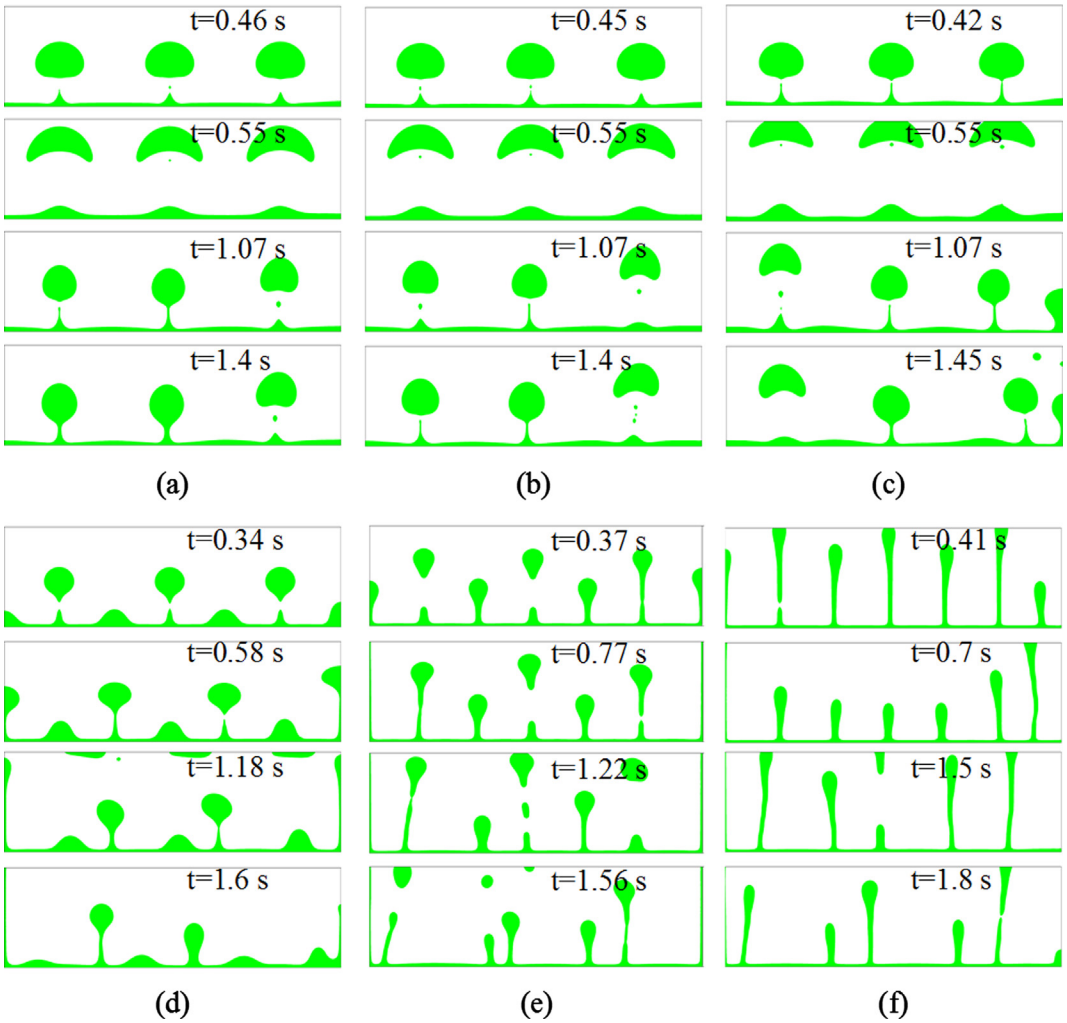

Fig. 14. Interface growth for different applied magnetic field intensities: (a) 0 kA/m; (b) 5 kA/m; (c) 10 kA/m; (d) 20 kA/m; (e) 30 kA/m and (f) 40 kA/m.

formation sites multiplies, the bubble departure time and the bubble departure diameter are both significantly reduced. In addition, after the bubble is detached, a long bubble belt begins to form between the bubble and the vapour film, and the bubble column begins to form at the left and right boundaries. When the bubble column is extended to a certain length under the combined action of gravity, surface tension and magnetic forces after a certain disturbance, the bubble column begins to break off and forms small bubbles. When the magnetic field intensity increases to 20 kA/m or 30 kA/m, both the bubble flow and bubble column flow exist simultaneously, as shown in Fig. 14(d)∼(e). When the magnetic field intensity reaches 40 kA/m, the bubble release pattern of film boiling has completely evolved into a tall and stable bubble column flow, as shown in Fig. 14(f).

Figs. 15 and 16 show the effect of the magnetic field intensity on the heat transfer characteristics of MNF film boiling. Fig. 15(a) and (b) show the variation in the space-averaged wall temperature and Nu number with time under different magnetic field intensities, respectively, and Fig. 16 depicts the variation in the space- and time-averaged wall temperature and Nu number with the magnetic field intensity. When the magnetic field intensity increases from 0 kA/m to 10 kA/m, the space-averaged wall temperature and Nu number show a periodicity over time, and there is no significant change in the period and amplitude. The space- and time-averaged wall temperature and Nu number remain basically unchanged with an increase in the magnetic field intensity, indicating that the low magnetic field intensity has little influence on the heat transfer characteristics of MNF film boiling. When the magnetic field intensity further increases to 20 kA/m, the vapour film wavelength decreases rapidly, the number of the bubble formation sites increases, and the bubble is detached randomly, losing periodicity. Therefore, the space-averaged wall temperature and Nu number are no longer periodic over time. The convection heat transfer between the wall and the fluid becomes more intense due to the random departure of the bubbles and the shorter bubble departure time. The heat transfer performance of the MNF is enhanced as a result. When the magnetic field intensity continued to increase to 40 kA/m, the bubble morphology changed greatly. Bubbles are no longer directly detached from the vapour film, and the flow pattern of film boiling is the vapour column flow. Because of the formation of a continuous vapour column, the thickness of vapour film is always at a minimum. As a result, the thermal resistance between the wall surface and the phase interface is always at a minimum, so the heat transfer is always at the strongest state, and the space-averaged wall temperature and Nu number are basically unchanged over time. In conclusion, when the magnetic field intensity is small, the heat transfer characteristics of film boiling are periodic and the magnetic field intensity has little effect on the heat transfer. When the magnetic field intensity increases to a certain value, the heat transfer characteristic no longer has periodicity, and with an increase in the magnetic field intensity, the heat transfer is significantly enhanced.

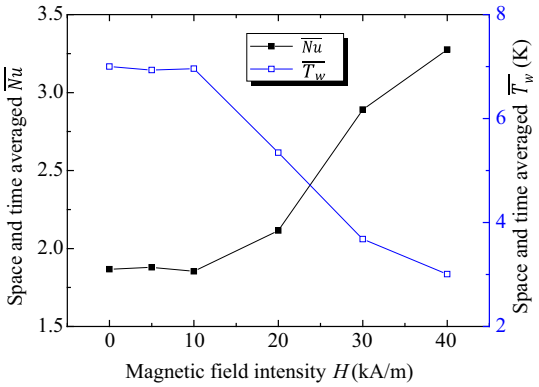

Fig. 16. Space- and time-averaged Nusselt number and wall temperature with different applied magnetic field intensities.

4.3. Effect of magnetic susceptibility

Fig. 17 shows the evolution of the phase interface under different magnetic susceptibilities, and Figs. 18 and 19 displays the effect of the magnetic susceptibility on the heat transfer characteristics of MNF film boiling. Here, the magnetic field intensity is $H_0 = 10$ kA/m, and the volume concentration of the MNF is $\varphi = 0.1\%$. Fig. 18(a) and (b) show the variation in the space-averaged wall temperature and Nu number with time under different magnetic susceptibilities, respectively, and Fig. 19 depicts the variation in the space- and time-averaged wall temperature and Nu number with magnetic susceptibility. Nearly the same effects of the magnetic field intensity on the interface growth and heat transfer performance can be seen in Figs. 17–19 when increasing

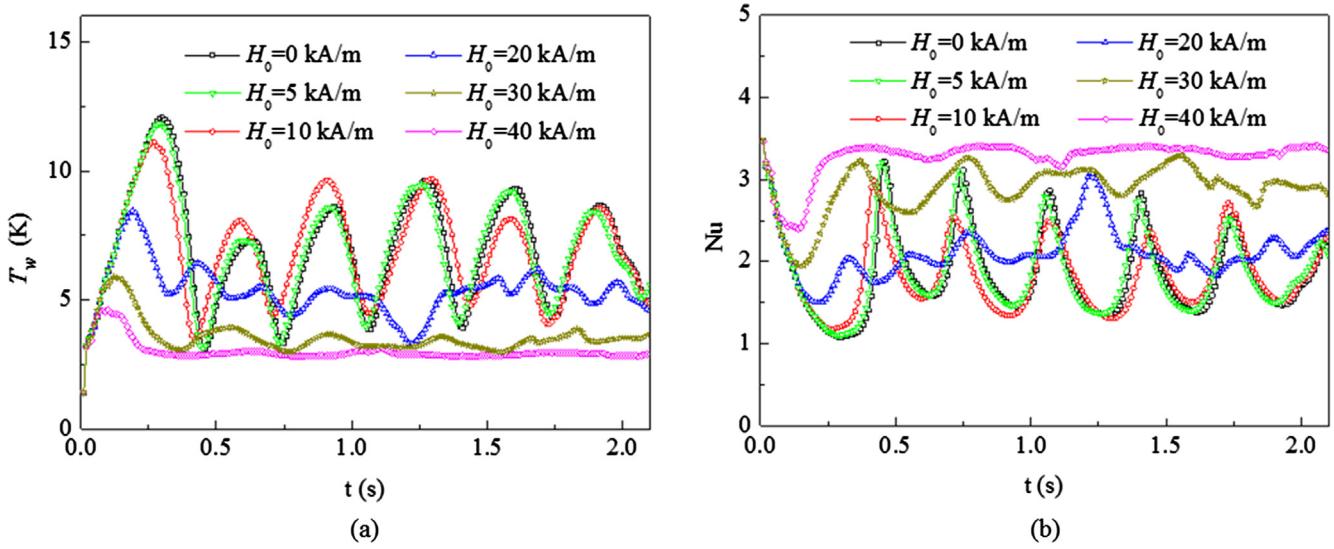

Fig. 15. Variation in the space-averaged (a) wall temperature and (b) Nusselt number for a varying magnetic field intensity.

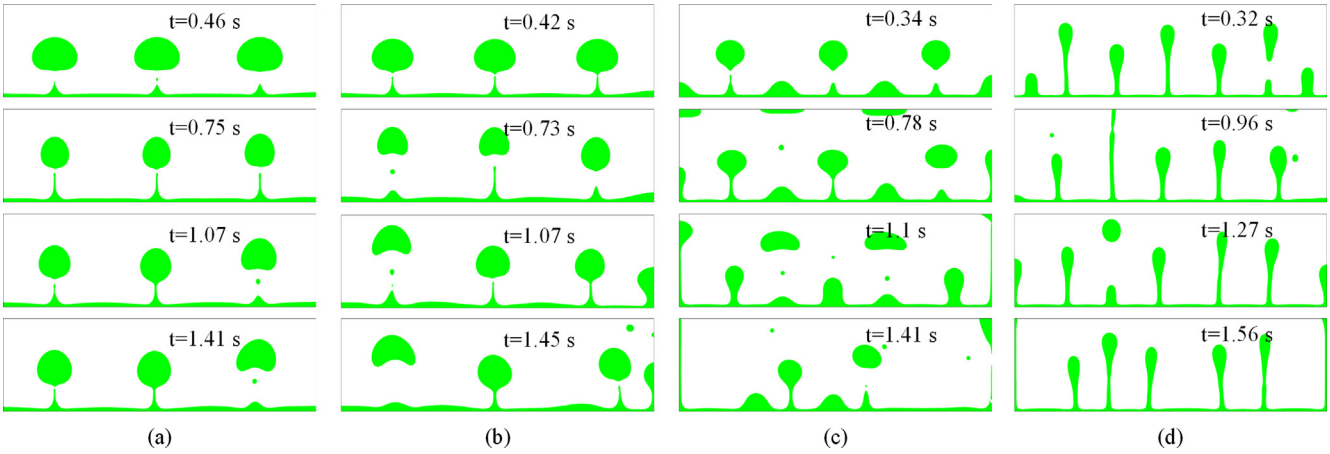

Fig. 17. Interface growth for different susceptibilities: (a) $\chi = 0$; (b) $\chi = 0.2$; (c) $\chi = 0.4$ and (d) $\chi = 0.8$.

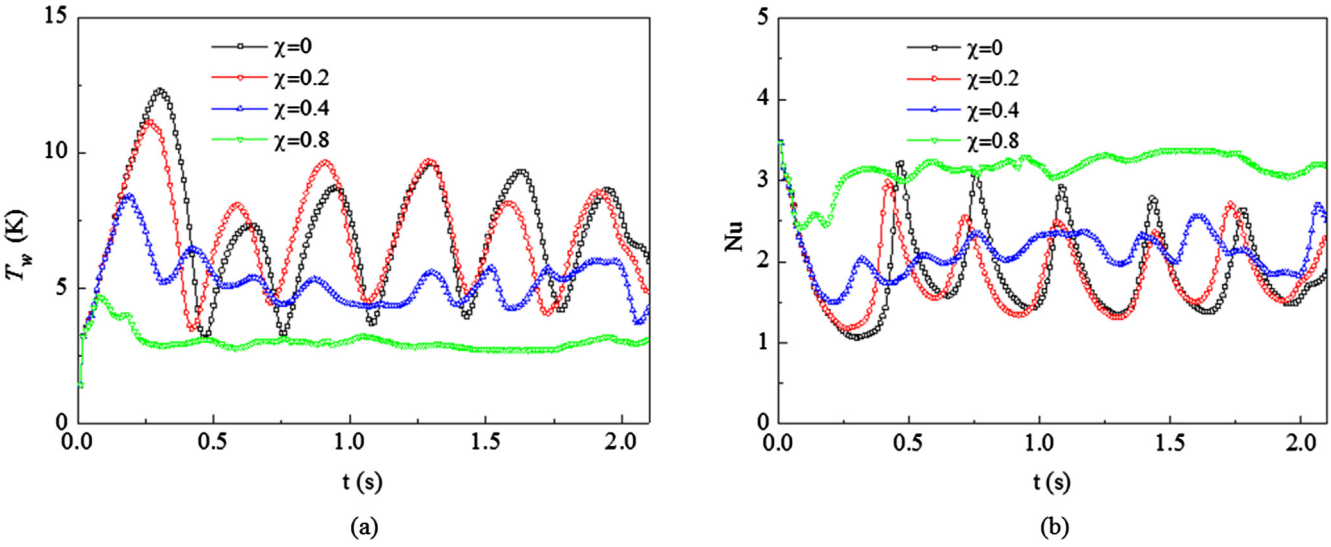

Fig. 18. Variation in the space-averaged (a) wall temperature and (b) Nusselt number for varying susceptibilities.

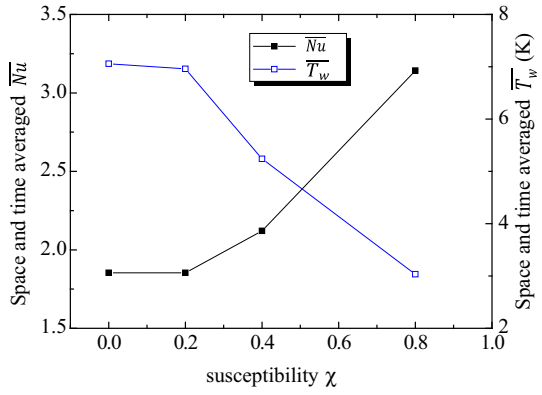

Fig. 19. Space- and time-averaged Nusselt number and wall temperature with different susceptibilities.

the susceptibility at a fixed magnetic field intensity. When the magnetic susceptibility is small, the heat transfer characteristics of film boiling are periodic, and the magnetic susceptibility has little effect on the heat transfer. When the magnetic susceptibility increases to a certain value, the heat transfer characteristic loses its periodicity, and the heat transfer performance is greatly enhanced with increasing magnetic susceptibility.

5. Conclusions

In this paper, the VOSET interface tracking method including the phase change effect was combined with Maxwell's equation and the momentum equation, which couples the surface tension and magnetic field force, and a two-dimensional numerical model for solving the problem of incompressible two-phase boiling of a MNF in presence of a magnetic field was established. The heat transfer characteristics of saturated film boiling of the MNF and the dynamic characteristics of the bubbles in presence of a uniform magnetic field were numerically simulated using the developed numerical model in the present study. The following conclusions were obtained.

(1) Under the condition of low volume concentration, the bubble departure time is shortened and the heat transfer performance of the MNF was slightly enhanced with increasing volume concentration.

(2) When the magnetic field intensity or magnetic susceptibility is small, there is no significant change in the evolution of the phase interface. With a further increase in the magnetic field intensity or magnetic susceptibility, the gradually increasing magnetic field intensity or magnetic susceptibility causes greater Maxwell stress, which renders the gas-liquid interface more unstable. The bubbles begin to deform in the direction of the magnetic field, the wavelength of the vapour film and the bubble size when released decreases, the bubble departure time shortens, and the number of bubble formation sites increases. Furthermore, bubble formation and departure become random, and both of the bubble flow and the bubble column flow exist simultaneously. When the magnetic field intensity or magnetic susceptibility increases to a certain value, the bubble is stretched along the magnetic field direction under the action of the magnetic force, further forming a vertical vapour column, which indicates that the bubble release pattern of film boiling has completely evolved into a bubble column flow.

(3) When the magnetic field intensity or magnetic susceptibility is low, the heat transfer characteristics of the MNF film boiling are periodic and have little effect on the heat transfer. However, when the magnetic field intensity or magnetic susceptibility increases to a certain value, the heat transfer characteristic no longer has periodicity, and the heat transfer performance is significantly enhanced with an increase in the magnetic field intensity or magnetic susceptibility.

Briefly, the numerical model of incompressible two-phase boiling of a MNF in presence of a magnetic field is developed in this paper, promoting the popularization and application of MNFs.

Conflict of interest statement

The authors declared that there is no conflict of interest.

Acknowledgements

The authors wish to acknowledge the support of the National Basic Research Program of China (973 Program) (Grant No. 2015CB251502) and the National Natural Science Foundation of China (U1738105).

References

[1] M. Bahiraei, M. Hangi, Flow and heat transfer characteristics of magnetic nanofluids: a review, J. Magn. Magn. Mater. 374 (2015) 125–138.
[2] M.A. Khairul, E. Doroodchi, R. Azizian, B. Moghtaderi, Advanced applications of tunable ferrofluids in energy systems and energy harvesters: a critical review, Energy Convers. Manage. 149 (2017) 660–674.
[3] J.H. Liu, J.M. Gu, Z.W. Lian, H. Liu, Experiments and mechanism analysis of pool boiling heat transfer enhancement with water-based magnetic fluid, Heat Mass Transf. 41 (2004) 170–175.
[4] J.H. Lee, T. Lee, Y.H. Jeong, Experimental study on the pool boiling CHF enhancement using magnetite-water nanofluids, Int. J. Heat Mass Transf. 55 (2012) 2656–2663.
[5] T. Lee, J.H. Lee, Y.H. Jeong, Flow boiling critical heat flux characteristics of magnetic nanofluid at atmospheric pressure and low mass flux conditions, Int. J. Heat Mass Transf. 56 (2013) 101–106.
[6] P. Naphon, Effect of magnetic fields on the boiling heat transfer characteristics of nanofluids, Int. J. Thermophys. 36 (2015) 2810–2819.
[7] M. Şeşen, Y. Tekşen, B. Şahin, K. Şendur, M. Pınar Mengüç, A. Koşar, Boiling heat transfer enhancement of magnetically actuated nanofluids, Appl. Phys. Lett. 102 (2013) 163107.
[8] A. Abdollahi, M. Reza Salimpour, Experimental investigation on the boiling heat transfer of nanofluids on a flat plate in the presence of a magnetic field, Eur. Phys. J. Plus 131 (2016).
[9] A. Abdollahi, M.R. Salimpour, N. Etesami, Experimental analysis of magnetic field effect on the pool boiling heat transfer of a ferrofluid, Appl. Therm. Eng. 111 (2017) 1101–1110.
[10] R. Amirzehni, H. Aminfar, M. Mohammadpourfard, Experimental study of magnetic field effect on bubble lift-off diameter in sub-cooled flow boiling, Exp. Therm Fluid Sci. 89 (2017) 62–71.
[11] M. Mohammadpourfard, H. Aminfar, M. Sahraro, Numerical simulation of nucleate pool boiling on the horizontal surface for ferrofluid under the effect of non-uniform magnetic field, Heat Mass Transf. 50 (2014) 1167–1176.
[12] M. Mohammadpourfard, H. Aminfar, M. Karimi, Numerical investigation of subcooled boiling characteristics of magnetic nanofluid under the effect of quadrupole magnetic field, J. Eng. Thermophys. 26 (2017) 427–446.
[13] H. Aminfar, M. Mohammadpourfard, R. Maroofiazar, Numerical study of non-uniform magnetic fields effects on subcooled nanofluid flow boiling, Prog. Nucl. Energy 74 (2014) 232–241.
[14] A. Malvandi, Film boiling of magnetic nanofluids (MNFs) over a vertical plate in presence of a uniform variable-directional magnetic field, J. Magn. Magn. Mater. 406 (2016) 95–102.
[15] M.H. Taheri, M. Mohammadpourfard, A.K. Sadaghiani, A. Kosar, Wettability alterations and magnetic field effects on the nucleation of magnetic nanofluids: a molecular dynamics simulation, J. Mol. Liq. 260 (2018) 209–220.
[16] H. Ki, Level set method for two-phase incompressible flows under magnetic fields, Comput. Phys. Commun. 181 (2010) 999–1007.
[17] M.R. Ansari, A. Hadidi, M.E. Nimvari, Effect of a uniform magnetic field on dielectric two-phase bubbly flows using the level set method, J. Magn. Magn. Mater. 324 (2012) 4094–4101.
[18] D.X. Shi, Q.C. Bi, R.Q. Zhou, Numerical simulation of a falling ferrofluid droplet in a uniform magnetic field by the VOSET method, Numer. Heat Transfer, Part A: Applicat. 66 (2014) 144–164.
[19] D.L. Sun, W.Q. Tao, A coupled volume-of-fluid and level set (VOSET) method for computing incompressible two-phase flows, Int. J. Heat Mass Transf. 53 (2010) 645–655.
[20] J.U. Brackbill, D.B. Kothe, C. Zemach, A continuum method for modeling surface tension, J. Comput. Phys. 100 (1992) 335–354.
[21] R.E. Rosensweig, Ferrohydrodynamics, Cambridge University Press, Cambridge, 1985.
[22] T. Wang, H.X. Li, Y.F. Zhang, W. Han, T.Y. Sheng, W.Q. Zhang, Numerical Simulation of Two-Phase Flows Using 3D-VOSET Method on Dynamically Adaptive Octree Grids, in: 2014 22nd International Conference on Nuclear Engineering, Prague, Czech Republic, 2014.
[23] D.L. Sun, Z.G. Qu, Y.L. He, W.Q. Tao, An efficient segregated algorithm for incompressible fluid flow and heat transfer problems—IDEAL (Inner Doubly Iterative Efficient Algorithm for Linked Equations) Part I: Mathematical formulation and solution procedure, Numer. Heat Transfer, Part B: Fundament. 53 (2008) 1–17.
[24] K. Ling, G. Son, D.L. Sun, W.Q. Tao, Three dimensional numerical simulation on bubble growth and merger in microchannel boiling flow, Int. J. Therm. Sci. 98 (2015) 135–147.
[25] H.S. Udaykumar, R. Mittal, W. Shyy, Computation of solid-liquid phase fronts in the sharp interface limit on fixed grids, J. Comput. Phys. 153 (1999) 535–574.
[26] G. Tryggvason, R. Scardovelli, S. Zaleski, Direct Numerical Simulations of Gas Liquid Multiphase Flows, Cambridge University Press, New York, 2011.
[27] D.X. Shi, Q.C. Bi, R.Q. Zhou, Numerical investigation on the evolution characteristics of two-phase interface in ferrofluids, J. Xi'an Jiaotong Univ. 48 (2014) 123–129.
[28] C. Flament, S. Lacis, J.C. Bacri, A. Cebers, S. Neveu, R. Perzynski, Measurements of ferrofluid surface tension in confined geometry, Phys. Rev. E 53 (1996) 4801–4806.
[29] V.V. Klimenko, Film boiling on a horizontal plate — new correlation, Int. J. Heat Mass Transf. 24 (1981) 69–79.